Research paper

Structure of CoFe$_2$O$_4$@CdTe nanocomposite with core/shell structure for high-performance Bi-modal imaging

CrossMark

Fujun Liu[a], Luce Vander Elst[a,b], Robert N. Muller[a,b], Sophie Laurent[a,b,*]

[a] Department of General, Organic and Biomedical Chemistry, NMR and Molecular Imaging Laboratory, University of Mons, Avenue Maistriau, 19, B-7000 Mons, Belgium
[b] Center for Microscopy and Molecular Imaging (CMMI), B-6041 Charleroi-Gosselies, Belgium

GRAPHICAL ABSTRACT
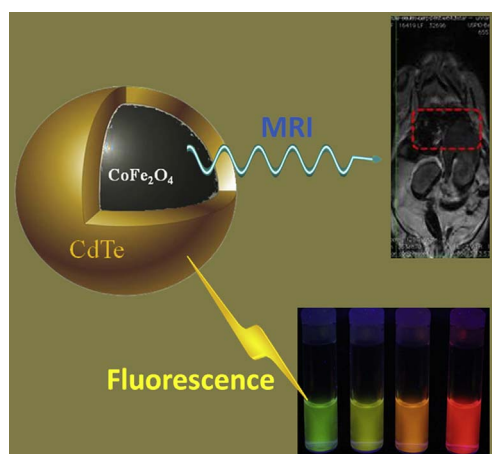
ARTICLE INFO

ABSTRACT

A novel bi-modal imaging contrast agent was fabricated by depositing a layer of CdTe on the surface of CoFe$_2$O$_4$ nanoparticle, and applications for optical-MRI bi-modal imaging were investigated. The core/shell structure of the obtained nanocomposite was verified by TEM. TGA and nuclear magnetic relaxation dispersion (NMRD) profiles were applied for the deposition study. The *in-vivo* and *in-vitro* results showed that the deposition of CdTe layer can evidently improve the relaxivity of CoFe$_2$O$_4$ nanoparticle, which was investigated and explained by a "cation migration" theory. The as-synthesized compound is a promising nanocomposite for high performance bi-modal imaging applications.

1. Introduction

During these decades, many imaging techniques have been invented for biological researches and clinical diagnoses, such as ultra-sonography [1–3], x-ray computed tomography (CT) [4–6], magnetic resonance imaging (MRI) [7–11], positron emission tomography (PET) [12–15] and optical imaging (OI) [16–19]. All these imaging techniques provide possibilities for clinicians to achieve the noninvasive imaging of patients' bodies. Due to the different principles, each imaging method has its own advantages and disadvantages. For example,

ultrasonography is popularly employed during pregnancy because of cheap price and safety forthe fetus, but the spatial resolution of the image is limited by the imaging depth: a lower frequency wave produces lower spatial resolution and deeper image depth into the body, while a higher frequency is capable of reflecting or scattering from smaller structures due to its shorter wavelength, which increases the spatial resolution but limits the depth of penetration of the sound wave into the body [20–24]. Analogously, MRI is widely used for its good contrast between different soft tissues of the body, no usage of ionizing radiation and high spatial resolution (100 μm), however, the long scanning time makes it impossible to perform the real-time detection [25]. On the other hand, optical imaging (OI), including bioluminescence imaging (BLI) and fluorescence imaging (FLI), is accessible, accurate, and specific, and can offer fast and sensitive whole-body imaging, even detecting microscopic tumors, and the spatial resolution is about 1–10 mm, dependent on the tissue depth [26]. Therefore, researchers started to combine different imaging techniques to avoid the disadvantages of each single technique, resulting in bi-modal imaging or multi-modal imaging.

There are increasing amount of publications on the preparation of bi-modal imaging techniques, including PET/CT [27–31] PET/MRI [32–34] and so on. The combining of two different imaging techniques firstly requires the design and fabrication of new-model combined scanner. The first report on the combining of PET and CT scanner was published on 1998 by Kinahan [28], where a Siemens/CTI ECAT 951R/31 PET tomography and a General Electric 9800 series CT scanner were combined to be a new PET/CT scanner. The PET and CT data can be collected simultaneously or independently, depending on the requirement of the test, and the PET data can be corrected by CT data to provide accurately registered anatomical localization of structures seen in the PET image. Compared with the images using a standard 3D PET scanner, it came to a conclusion that using CT information is a feasible way to obtain attenuation correction factors of 3D PET. The combination of PET and MRI was reported by Alpert on 1996. However, it was about the data analysis of PET and MRI followed by image registration of the two kinds of imaging techniques [35]. After 2005, up to three companies, including Koninklijke Philips N.V., Siemens AG and General Electric, declared the availability of their PET/MRI imaging devices. And at this moment, only Siemens AG could offer a fully integrated whole body and simultaneous acquisition PET/MRI system, which was approved by the FDA and released for customer purchase in 2011 [36]. The combination of MRI and OI was reported by Xu [37], where they made a new system for the study on small animal brains, using broadband near-infrared (NIR) tomography system coupled with MRI. MRI produced high-resolution tissue images, which were applied as *a priori* information in the NIR image reconstruction process, so the NIR images obtained were improved in terms of the quantitative accuracy and the spatial resolution, to provide a much more straightforward and intuitionistic tool for the study of cerebral physiology and pathophysiology.

On the other hand, some imaging techniques need contrast agents (CAs) to obtain high-quality images, such as PET, CT and MRI. So the combining of different contrast agents is needed to prepare bi-modal or multi-modal imaging contrast agents, for the aim of multi-mode imaging. The preparation of bi-functional contrast agents became a popular topic for researchers of material science and chemistry. There is one issue needed to pay attention, the influences on the contrast effect of each component after the combination. Bimodal contrast agents for MR imaging and optical imaging were prepared by Daldrup-Link, using Gadophrin-2 composed of a porphyrin ring and two covalently linked gadolinium chelates [38]. With a molecular weight of 1759.38 Da, gadophrin-2 had an r_1 relaxivity of 19.8 $s^{-1}mmol^{-1}$ and an r_2 relaxivity of 30.0 $s^{-1}mmol^{-1}$ at 20 MHz and 37 °C, due to the existence of two Gd^{3+} ions. The porphyrin ring provides fluorescence to the obtained hybrid, with an excitation wave length of 499 nm and a maximal emission at 617 nm. The *in vivo* cell tracking studies showed that

Gadophrin-2, as a cell marker, worked well on integrating the advantages of the two imaging techniques, where fluorescence imaging can provide an overview of the *in vivo* distribution of all transplanted major and minor cell subpopulations and MRI can specify the accumulation of major cell populations in host organs with sub-millimeter anatomical resolution. It is to be noted that the three-dimensional data sets provided by MRI and the two-dimensional data sets from fluorescence imaging did not show any influence on each other, but cooperated to localize transplanted cells more exactly and more deeply within tissues. Because of the excellent optical properties of quantum dots (QDs), including their photo-stability and their narrow and tunable emission spectrum, QDs were employed for the preparation of MRI/OI contrast agents. Mulder reported the synthesis of a new bimodal imaging probe, using CdSe/ZnS QDs coated with a paramagnetic gadolinium diethylenetriamine-pentaacetic acid (Gd-DTPA) layer [39]. However for the T_2 MRI, the study on the combination of magnetic ferrites and QDs was not widely reported [40–45]. Therefore, in this article we will focus on a novel MRI/OI contrast agent, made of a combination of $CoFe_2O_4$ nanoparticles and CdTe QDs.

2. Materials and methods

2.1. Materials

Distilled water was used to prepare all aqueous solutions. Cadmium chloride ($CdCl_2$), sodium telluride (Na_2TeO_3), sodium citrate, 3-mercaptopropionic acid (3-MPA), sodium borohydride ($NaBH_4$) and thioglycolic acid (TGA) were purchased from Sigma Chemical (Bornem, Belgium). Iron (III) chloride hexahydrate ($FeCl_3 \cdot 6H_2O$), cobalt chloride hexahydrate ($CoCl_2 \cdot 6H_2O$), sodium citrate, 1, 10-phenanthrolin (99%) and hydroxylamine hydrochloride ($NH_2OH \cdot HCl$) were purchased from Sigma Chemical (Bornem, Belgium). All other reagents and solvents were purchased from Aldrich Chemical (Bornem, Belgium) and were of the highest grade commercially available.

2.2. Methods

$CoFe_2O_4$ nanoparticles were synthesized as described in ref [46]. After measuring the concentrations of Co and Fe, 20 mL $CoFe_2O_4$ colloid with the total concentration of Co and Fe [Co + Fe] of 1.25 mM was put in a flat bottom beaker with 0.5 mL of 0.2 M $CdCl_2$, 50ug sodium citrate, 61 μL 3-MPA, 0.25 mL of 0.1 M Na_2TeO_3 and 31.25 mg $NaBH_4$ under magnetic stirring, followed by subsequent stirring for another one hour. This mixture was then poured into Teflon-coated bottle and heated in an autoclave at 140 °C for 1 h. The obtained colloid was dialyzed for 24 h, and then acetone was added (acetone/water = 1/4), followed by centrifugation at 10000 rpm for 1.5 h to separate free CdTe which was formed by homogeneous nucleation and was not loaded on the surface of $CoFe_2O_4$. The $CoFe_2O_4@CdTe$ was deposited on the bottom of the tube, and re-dispersed in acetone/water mixture and the centrifugation was repeated for three times. The purified $CoFe_2O_4@CdTe$ solid was then mixed with 0.5 mL 0.2 M $CdCl_2$, 50 mg sodium citrate, 61 μL 3-MPA, 0.25 mL 0.1 M Na_2TeO_3 and 31.25 mg $NaBH_4$, stirring at 140 °C for 1 h, and this step was repeated 1–5 times. The obtained products were purified by dialysis for 24 h, and placed in dark for characterizations. The products were named as $CoFe_2O_4@CdTe1$, $CoFe_2O_4@CdTe2$, $CoFe_2O_4@CdTe3$, $CoFe_2O_4@CdTe4$ and $CoFe_2O_4@CdTe5$, and the number after CdTe denote the CdTe deposition time.

TEM images were collected on a Tecnai 10 (FEI, Hillsboro, USA) with operating voltage at 200 kV. The hydrodynamic size and surface potential of all nanoparticles were measured on Zetasizer Nano Series Zen 3600 (Malvern, Worcestershire, United Kingdom), where 1 mL sample solution of about 2 mM was put in the cell, and measured at 37 °C.

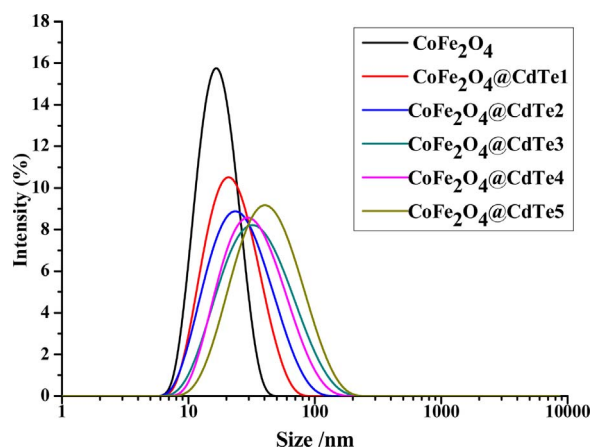The thermal stabilities of the absorptive surface active agents were

Fig. 1. The size change of CoFe$_2$O$_4$@CdTe with different CdTe depositions. The hydrodynamic diameter of the employed CoFe$_2$O$_4$@CdTe nanoparticles was 17.72 nm, which increased to 23.92, 36.11, 32.30, 33.43 and 38.72 nm when CdTe was deposited on CoFe$_2$O$_4$ surface, respectively.

Fig. 2. TEM pictures of CoFe$_2$O$_4$@CdTe nanocomposite.

studied by thermogravimetric analysis (TGA) with a TGA Q5000 (TA Instruments Ltd, New Castle, USA), which was made in an inert nitrogen atmosphere, providing an insight into the carbonization process. The optical properties were achieved by a LS-55 spectrofluorometer (Perkin-Elmer, Waltham, USA).

To study the magnetic properties of the nanoparticles obtained, r_1 and r_2 were measured on MiniSpec mq-20 (20 MHz) and mq-60 (60 MHz) (Bruker, Ettlingen, Germany), nuclear magnetic relaxation dispersion (NMRD) profiles were performed on Spinmaster-FFC 2000 relaxometer (Stelar, Mede, Italy). The MR images of the prepared CoFe$_2$O$_4$@CdTe were taken on a 300 MHz 7T Bruker Pharmascan imaging system (Ettlingen, Germany), equipped with the microimaging device (Micro2.5AHS/RF, 25 mm coil).

3. Results and discussion

3.1. Fabrication of CoFe$_2$O$_4$@CdTe nanocomposite

The size change of CoFe$_2$O$_4$@CdTe with increasing CdTe deposition was monitored by photon correlation spectroscopy (PCS), and the results are shown in Fig. 1. It can be found that the hydrodynamic diameter of CoFe$_2$O$_4$@CdTe increased as CdTe was deposited on the surface, and such increase continued with repeating the CdTe deposition process. After 5 times of CdTe depositions, the size of nanoparticles increased from 17.72 nm up to 38.72 nm. During the synthesis of CoFe$_2$O$_4$@CdTe, CdTe QDs were deposited on the surface of CoFe$_2$O$_4$ by *in situ* deposition. The normal difficult issue for the synthesis of hybrid materials is the "mismatch" of crystal lattices from the two components. For the epitaxial growth of one material on another, the interface translational symmetry should be considered. Lattice match, defined as the compatibility between the interface translational symmetry and the symmetry on both sides of the interface [47], is a very similar idea to the concept of coincidence-site lattices [48–51], which plays an important role in high angle grain boundaries. While, if the interface between two different materials cannot achieve such an exact match, there will be some finite mismatch of crystal lattices [52,53]. This finite mismatch compels researches to adopt strategies to avoid the separation of two materials. It is generally employed to use an amorphous layer between the two materials, acting as a "lubricant".

As the CoFe$_2$O$_4$ nanoparticles were synthesized by coprecipitation, followed by treatment with dilute nitric acid, the surface of CoFe$_2$O$_4$ nanoparticles had been etched by nitric acid to be amorphous and coated by sodium citrate. So this amorphous layer can be assumed as the substrate for the growth of CdTe. To prove this assumption, TEM pictures were recorded to show the structure of obtained CoFe$_2$O$_4$@CdTe nanocomposite, as shown in Fig. 2. The nanocomposite

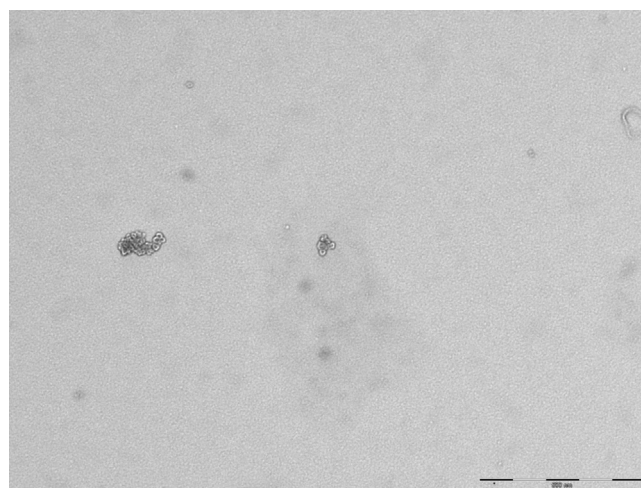showed a clear core/shell structure, with CoFe$_2$O$_4$ as the core and CdTe with the outward shell. However, there were some "blank" spaces between the core and shell, which was assumed to be the attached 3-MPA and sodium citrate [54–56]. With the help of the analysis software iTEM, the diameter of the core and the entire nanocomposite were 9.66 ± 2 nm and 24.18 ± 2 nm, respectively, with the shell thickness of 4.69 ± 0.5 nm. The existence of 3-MPA and sodium citrate had been confirmed by TGA analysis, as shown in Fig. 3. Since 3-MPA is liquid at room temperature, and TGA measurements are not allowed, only sodium citrate was used as the reference. The shape of the TGA curve for CoFe$_2$O$_4$@CdTe shows some similarities with that for sodium citrate, suggesting the presence of the attached surfactants [57,58].

Besides the heterogeneous growth on the surface of CoFe$_2$O$_4$, CdTe also presented homogeneous growth to form "free" CdTe particles, which will further grow bigger during the followed repeated CdTe-deposition processes. The presence of free CdTe will lead to two disadvantages, hindering the deposition of CdTe on CoFe$_2$O$_4$ and effecting the final imaging results. Therefore, separations of free CdTe from the solution were done during each purification procedure, to maximize the yield of heterogeneous growth of CdTe on CoFe$_2$O$_4$ surface.

3.2. Magnetic properties of CoFe$_2$O$_4$@CdTe nanocomposite

To investigate the influence of loaded CdTe on the magnetic properties of CoFe$_2$O$_4$ cores, the deposition of CdTe was repeated for 1–5 times, and the relaxivities of obtained nanocomposites were measured
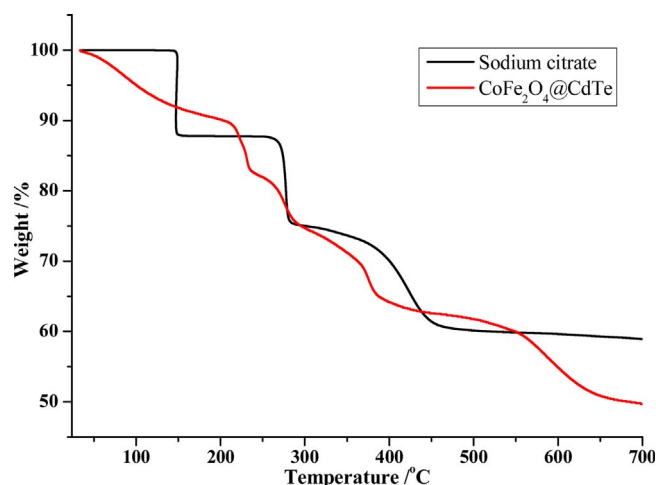

Fig. 3. The TGA curves of sodium citrate and CoFe$_2$O$_4$@CdTe.

Table 1

Longitudinal and transverse relaxivities of CoFe$_2$O$_4$@CdTe at 20 MHz and 60 MHz. The CoFe$_2$O$_4$ nanoparticles used for all the 6 samples were the same, d = 17.72 nm by DLS.

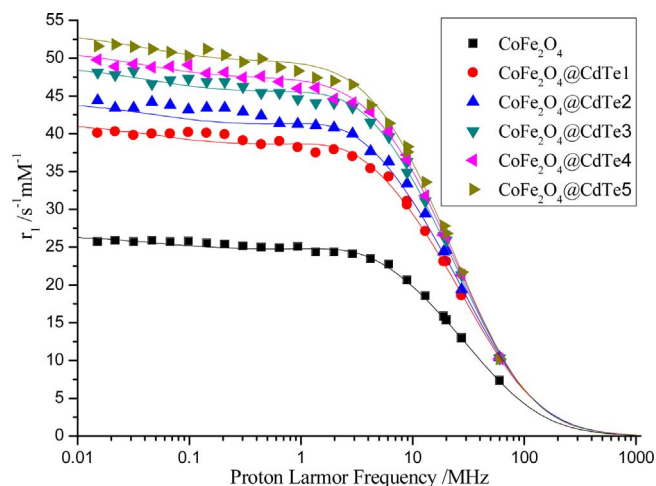| Sample	20 MHz			60 MHz		
	r_1 s^{-1}mM^{-1}	r_2 s^{-1}mM^{-1}	r_2/r_1	r_1 s^{-1}mM^{-1}	r_2 s^{-1}mM^{-1}	r_2/r_1
CoFe$_2$O$_4$	15.37	34.77	2.26	7.35	35.75	4.86
CoFe$_2$O$_4$@CdTe1	23.14	59.91	2.59	10.45	64.12	6.14
CoFe$_2$O$_4$@CdTe2	24.62	67.28	2.73	10.36	73.35	7.08
CoFe$_2$O$_4$@CdTe3	25.97	74.16	2.86	10.25	76.33	7.44
CoFe$_2$O$_4$@CdTe4	26.42	77.26	2.92	10.19	79.32	7.78
CoFe$_2$O$_4$@CdTe5	26.76	81.11	3.03	10.17	84.85	8.34

Fig. 4. NMRD profiles of CoFe$_2$O$_4$ and CoFe$_2$O$_4$@CdTe with 1–5 times of CdTe deposition, with fitting of each sample. The hydrodynamic diameter for the CoFe$_2$O$_4$ cores was 17.72 nm.

on MiniSpec mq-20 and mq-60 at 20 MHz and 60 MHz, respectively. Relaxivities are reported with respect to the total molarity of iron and cobalt (i.e., s^{-1}mM^{-1} Fe + Co) and the results are shown in Table 1. It is found that before the deposition of CdTe, CoFe$_2$O$_4$ nanoparticles had relatively low relaxivities, r_1 of 15.37 and 7.35 s^{-1}mM^{-1} at 20 and 60 MHz, respectively, and r_2 of 34.77 and 35.75 s^{-1}mM^{-1} at 20 and 60 MHz, respectively. When CdTe was deposited on the surface of CoFe$_2$O$_4$ nanoparticles, the relaxivities of the formed compound increased significantly, as r_2 increased to 59.91 and 64.12 s^{-1}mM^{-1} at 20 and 60 MHz, respectively. And as repeating the experiment process to deposit more CdTe on the surface of CoFe$_2$O$_4$ nanoparticles, the relaxivities continued to increase a little bit.

The increase of relaxivity $r_{1,2}$ after the deposition of CdTe can be explained by some effects of the deposition of CdTe on the surface state of CoFe$_2$O$_4$ nanoparticles, and subsequence on the relaxivity. Besides the particle size, the distribution of the iron and cobalt ions in the A and B sites strongly determines the relaxivity of CoFe$_2$O$_4$. And even a small change in the cationic distribution may result in substantial change of the magnetic moments and of the relaxivity [59]. Cannas reported the synthesis of silica coated cobalt ferrite [60], where three cobalt ferrite-silica nanocomposite samples with different silica contents were employed for the magnetic measurements. It was found that the coating of silica can increase the saturation magnetization Ms, and the higher silica content resulted in the higher Ms value. This phenomenon was explained by the author as a result of the change of cationic distribution, because of the loading of silica on the surface of CoFe$_2$O$_4$. Similarly, the change of relaxivity of CoFe$_2$O$_4$ can also be explained by this hypothesis. The Ms value of CoFe$_2$O$_4$ is strongly dependent on the inversion degree x [61], which can be calculated by the equation:

$$x = (1/4) \times [7-(\mu_{FU}/\mu_B)] \tag{1}$$

where μ_{FU} is the magnetic moment per unit formula, with the unit of μ_B.

The magnetic moments for Co^{2+} and Fe^{3+} ions are 3 μ_B and 5 μ_B, respectively, and the μ_{FU} is decided by the distribution of Co^{2+} and Fe^{3+} ions in tetrahedral (T) or in octahedral (O) coordination. For example, when two Fe^{3+} ions are in the O site and one Co^{2+} is in the T site, this structure is called direct spinel ($x = 0$) and the moment is $\mu_{FU} = 7 \mu_B$, while if one Fe^{3+} and one Co^{2+} are in the O site and one Fe^{3+} in the T site, this structure is called inverse spinel ($x = 1$) and the moment is $\mu_{FU} = 3 \mu_B$ [62]. The experimental data for μ_{FU} normally are between the two theoretical values. So it can be assumed that when CdTe is deposited on the surface of CoFe$_2$O$_4$ nanoparticles, the cationic distribution is changed, where more Fe^{3+} ions "move" from T to O site, resulting in the increase of μ_{FU} and decrease of the inversion degree x, which gives rise to the increase of the saturation magnetization Ms values. Based on the "static dephasing regime" (SDR), first introduced by Yablonskiy and Haache [63], the value of $r_{1/2}$ is proportional to the saturation magnetization of the sphere. Therefore, after the loading of CdTe on the surface of CoFe$_2$O$_4$ nanoparticles, the values of relaxivity (both r_1 and r_2) showed a great increase and such increase continued as more CdTe was deposited on CoFe$_2$O$_4$.

The increase of the relaxivities of CoFe$_2$O$_4$@CdTe, depending on the numbers of deposition of CdTe, can also be seen in the corresponding nuclear magnetic relaxation dispersion (NMRD) profiles, as shown in Fig. 4. NMRD measurements provide a valuable tool for separating the different relaxation mechanisms and dynamic processes influencing the relaxivity. In addition to the increase of the relaxivity values for the obtained CoFe$_2$O$_4$@CdTe after the deposition of CdTe, corresponding to the above discussion, the shape of the NMRD curve is also considerably important for the analysis of tested sample. In Fig. 4, the NMRD curves for CoFe$_2$O$_4$ and CoFe$_2$O$_4$@CdTe are in similar shape, but with different intensities. After fitting using a theoretical program developed in the laboratory, the saturation magnetization Ms shows an increase as a function of CdTe deposition (see Fig. 5). It can be found that after the deposition of CdTe on the surface, the Ms of CoFe$_2$O$_4$ drastically increased from 35.2 to 41.7 s^{-1}mM^{-1}, and continued to increase slightly from 41.7 to 42.5 s^{-1}mM^{-1} with repeating the CdTe deposition process for more times, which matched with the above assumption.
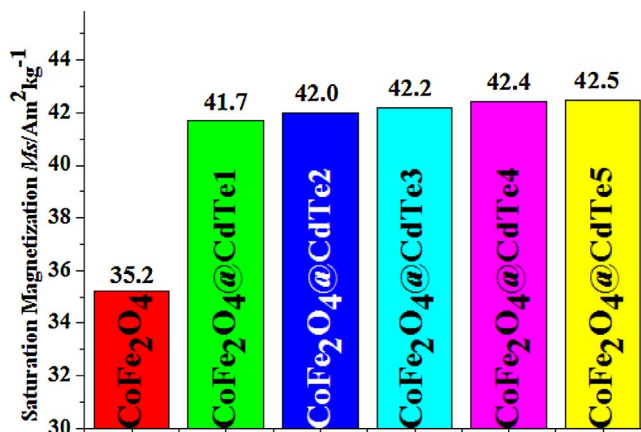

Fig. 5. The fitting results of NMRD data of the above samples.

3.3. Optical properties of CoFe₂O₄@CdTe

The optical properties of CdTe QDs was systematically studied in ref [64], where it was found that the emission wavelength of obtained CdTe QDs was dependent on the particle size, which can be tuned by adjusting experimental parameters, including the reaction temperature T and heating time t. And the fluorescence intensity was enhanced when excess Cd^{2+} ions were used, as a result of the formation of Cd-MPA (3-mercaptopropionic acid) complex on the surface of CdTe QDs. In this paper, CdTe was loaded on the surface of $CoFe_2O_4$ nanoparticles by *in situ* deposition, so it is very important to study the optical properties of the prepared $CoFe_2O_4$@CdTe, to check whether the coated $CoFe_2O_4$ nanoparticles had some influences on the optical properties of CdTe.

Firstly, it was studied whether the initial concentration of $CoFe_2O_4$ nanoparticles can affect the optical properties of obtained $CoFe_2O_4$@CdTe product. 0.5–10 mL of 1 M $CoFe_2O_4$, 0.5 mL of 0.2 M $CdCl_2$, 0.25 mL of 0.1 M Na_2O_3Te, 61uL 3-MPA and 32 mg $NaBH_4$ were mixed up to 20 mL and placed into the autoclave, which was heated at 140 °C for 2 h. The purification process was done as described above Then all the samples were diluted to make the samples with the same $CoFe_2O_4$ concentration, followed by testing the emission spectra. The emission curves of $CoFe_2O_4$@CdTe samples with different $CoFe_2O_4$ initial concentrations are shown in Fig. 6. It is found that as the volume of $CoFe_2O_4$ increased from 0.5 to 3 mL (the initial concentration from 25 to 150 mM), it induced a red-shift from 600 to 623 nm of the emission fluorescence, and the maximum wavelength shifted back to ∼600 nm when the initial concentration of $CoFe_2O_4$ nanoparticles continued to increase from 0.15 M to 0.4 M. Therefore, the initial $CoFe_2O_4$ concentration was fixed at 0.15 M as the optimum condition during the following experiments.

As the optimal initial concentration of $CoFe_2O_4$ nanoparticles was fixed, it was investigated how to influence the optical properties when the CdTe deposition process was repeated several times to load more CdTe on the surface of $CoFe_2O_4$ nanoparticles. With the help of photon correlation spectroscopy (PCS), the size analysis showed that the hydrodynamic diameter of $CoFe_2O_4$ nanoparticles was 17.72 nm, and after the CdTe deposition for five times, the obtained $CoFe_2O_4$@CdTe5 had a hydrodynamic diameter of 38.72 nm, The PL spectra are shown in Fig. 7. After the first CdTe deposition on the surface of $CoFe_2O_4$, Cd and Te ions were easier to crystallize on $CoFe_2O_4$ surface, as there already existed CdTe crystal, which made it more apt to originate homogeneous nucleation [65]. As described above, the amorphous layer on the surface of $CoFe_2O_4$ nanoparticles made it possible for the heterogeneous nucleation of CdTe to take place and crystallize on $CoFe_2O_4$ surface
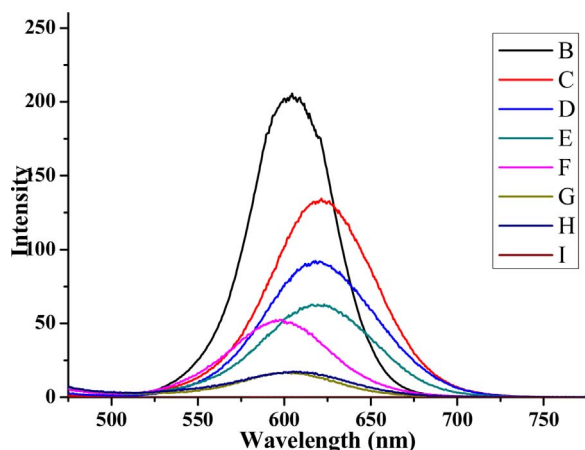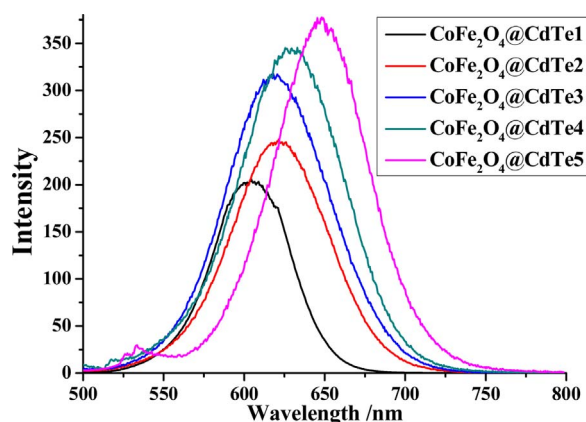
Fig. 7. Emission spectres of vavious CoFe2O4@CdTe (λ_{ex} = 450 nm, slit$_{ex}$ = slit$_{em}$ = 4 nm).

[60]. On the other hand, the homogeneous nucleation also occurred to form unattached CdTe QDs in the reaction solution, which were separated from the colloid after purification and separation using high speed centrifugation. So when more Cd^{2+} and TeO_3^{2-} ions were added in to the reactor, homogeneous nucleation of CdTe took place on $CoFe_2O_4$ surface, using earlier formed CdTe as the "seed". As increasing the loading of CdTe, the PL intensity of obtained compound increased and the emission peak shown red-shift. The red-shift was assumed to be caused by the increase of the depth of loaded CdTe layer, and the increase of fluorescence intensity was caused by the increase of the quantity of loaded CdTe as repeating the CdTe deposition process.

3.4. Imaging study

The main aim of the prepared $CoFe_2O_4$@CdTe nanoparticles is their use in medical imaging. To probe this feature, we did *in vivo* imaging experiments to study the imaging effect of the obtained product.

The cobalt ferrite $CoFe_2O_4$ and cadmium telluride coated cobalt ferrite $CoFe_2O_4$@CdTe contrast agents were used for the *in vitro* studies. Particle sizes were determined in triplicate at 37 °C with a laser light-scattering submicron particle size analyzer PCS, and four samples were chosen for the *in vitro* imaging, $CoFe_2O_4$ nanoparticles with hydrodynamic diameters of 12.50, 21.33 and 46.74 nm (denoted as $CoFe_2O_4$-12, $CoFe_2O_4$-21 and $CoFe_2O_4$-46, respectively) and $CoFe_2O_4$@CdTe with the hydrodynamic diameters of $CoFe_2O_4$ core being 21.33 nm, at overall concentrations of 0.4, 0.8 and 1.6 mM. Each sample was placed into a small plastic tube. Distilled water was employed as the reference.

The T_1-weighted and T_2-weighted MR images of the four samples for *in vitro* studies are shown in Figs. 8 and 9, respectively. The T_1 values were measured using inversion-recovery fast spin-echo sequences ($TR/TE/TI$ = 2200/18/50, 100, 200, 500, 800, 1200 and 2100 ms, where TI refers to inversion time) while varying the T_1 and keeping the TR and TE constants, following these:

$$M_{Before\_IR} = M_0(1-e^{-T_{SP\_to\_Before\_IR}/T_1}) \tag{2}$$

$$M_{acq} = M_0[(1-e^{-TI/T1})-f_{inv}\cdot(1-e^{-TSP\_to\_Before\_IR/T1})\cdot e^{-TI/T1}] \tag{3}$$

where M_{Before_IR} is the longitudinal magnetization right before the application of the nonselective inversion RF pulse, M_0 is the longitudinal magnetization under fully relaxed conditions, $T_{SP\_to\_Before\_IR}$ is the time between the end of the dual gradient spoiler and the application of the nonselective RF pulse, M_{acq} is the longitudinal magnetization right before the 90° acquisition RF pulse is applied, and f_{inv} is the effective spin inversion fraction [67,68]. For T_1-weighted MRI, the brightness of an image is inversely proportional to the value of T_1, and directly proportional to the value of longitudinal relaxation rate R_1. The T_1 for water is 3.54 s (T = 37 °C), and its image is absolutely dark under the T_1-weighted MRI. When contrast agents are added, the T_1 is shorter and

Fig. 6. The emission spectra of CoFe2O4@CdTe with the same CoFe2O4 concentration (curves B-I were assigned to the samples with various volumes of CoFe2O4, 0.5, 1, 2, 3, 4, 5, 8 and 10 mL, respectly. λ_{ex} = 450 nm, slit$_{ex}$ = slit$_{em}$ = 4 nm).
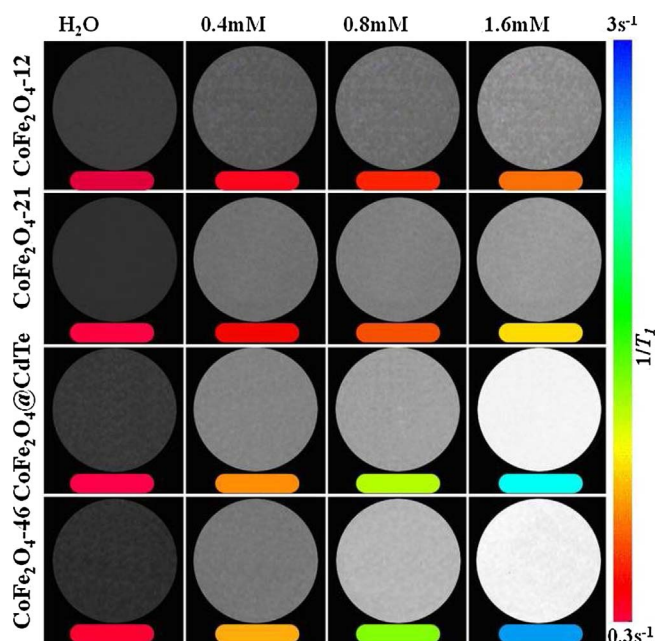
Fig. 8. The T_1-weighted MR images and their color maps of CoFe$_2$O$_4$@CdTe and CoFe$_2$O$_4$ nanoparticles with different hydrodynamic diameters.
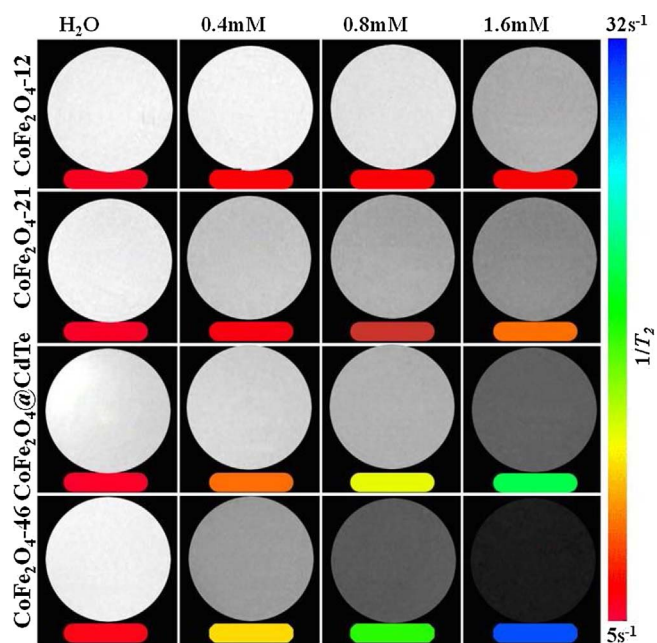

Fig. 9. The T_2-weighted MR images and their color maps of CoFe$_2$O$_4$@CdTe and CoFe$_2$O$_4$ nanoparticles with different hydrodynamic diameters.

the obtained image turns "whiter" [69]. As shown in Fig. 8, it can be found that the images got whiter when contrast agents were present, and brightness of MR images increased with the concentration of contrast agents. The corresponding color map under each T_1-weighted image shows the change of the longitudinal relaxation rate R_1, and the bluer one represented larger R_1 (shorter T_1). The value of R_1 is dependent on the relaxivity r_1, following this equation:

$$R_i = R_{iwater} + r_i[M], i = 1, 2 \tag{4}$$

where [M] is the concentrantion of contrast agents and R_{iwater} is the relaxation rate of pure water. So when the concentration of contrast agents increases from 0.4 to 1.6 mM, the R_1 shows a linear increase and the images are brighter. As described above, the coating of CdTe on the

surface induces an increase of the relaxivity of CoFe$_2$O$_4$ nanoparticles, as well as the diameter does. Therefore, with the same concentration, bigger CoFe$_2$O$_4$ nanoparticles gave rise to whiter MR image, and the MR images of CoFe$_2$O$_4$@CdTe were whiter than those of CoFe$_2$O$_4$ with the same core diameter.

Similar phenomena happened to the T_2-weighted MR images of the same samples. The T_2 values were measured using conventional spin-echo (TR/TE = 2000 ms/10, 15, 20, 25, 30, 40, 50, 60 and 70 ms) and gradient-echo sequences (TR/TE = 1000 ms/4, 11, 18, 25, 32, and 39 ms) with one echo for each sequence while varying the TE, and were calculated by fitting the signal intensities with increasing TEs into a mono-exponential function [70], following this equation:

$$M_{xy}(t) = M_{xy}(0)e^{-t/T2} \tag{5}$$

where $M_{xy}(0)$ and $M_{xy}(t)$ are the initial and time = t transverse magnetization. Different to the T_1-weighted image, the brightness of T_2-weighted image is directly proportional to the value of T_2, and inversely proportional to the value of longitudinal relaxation rate R_1. So the increase of spin–spin relaxation rate R_2, caused by the increase of either the transverse relaxivity r_2 or the diameter of CoFe$_2$O$_4$ nanoparticles, resulted in darker MR images, as shown in Fig. 9. After the coating of CdTe, the r_2 of CoFe$_2$O$_4$ increased a lot, so the T_2-weighted MR images of CoFe$_2$O$_4$@CdTe were much darker that those of CoFe$_2$O$_4$ with the same core diameter. By comparing Eq (2), Eq (4) and Eq (5), the different increase rates of r_1 and r_2 as a function of Ms.

4. Conclusions

Bi-modal CoFe$_2$O$_4$@CdTe nanoparticles have been synthesized through *in situ* deposition of CdTe on the surfaces of CoFe$_2$O$_4$ nanoparticles. It was found that the relaxivities of CoFe$_2$O$_4$@CdTe showed remarkable increase, compared with the CoFe$_2$O$_4$ nanoparticles before the CdTe deposition. This increase of relaxivities was explained with a "cation-distribution" mode. It was assumed that after the coating of CdTe, the saturation magnetization Ms of the nanoparticle was increased as a result of the change of the cationic distribution, where more Fe^{3+} ions "moved" from T to O site and the structure of CoFe$_2$O$_4$ turned more "direct spinel". The in vitro MR imaging proved that the deposition of CdTe on the surface of CoFe$_2$O$_4$ nanoparticles had successfully enhanced the performance as the MRI contrast agents.

Acknowledgements

References

[1] R.J. Adams, V.C. McKie, L. Hsu, B. Files, X. Vichinsky, et al., Alpha thalassemia is associated with decreased risk of abnormal transcranial Doppler ultrasonography in children with sickle cell anemia, N. Engl. J. Med. 339 (1998) 5–11.

[2] C.L. Moore, J.A. Copel, Point-of-care ultrasonography, N. Engl. J. Med. 364 (2011) 749–757.

[3] W.H. Cooner, B.R. Mosley, C.L. Rutherford, J.H. Beard, H.S. Pond, W.J. Terry, T.C. Igel, D.D. Kidd, Prostate cancer detection in a clinical urological practice by ultrasonography, digital rectal examination and prostate specific antigen, J. Urology 167 (2002) 966–973.

[4] M. Dierolf, A. Menzel, P. Thibault, P. Schneider, C.M. Kewish, et al., Ptychographic X-ray computed tomography at the nanoscale, Nature 467 (2011) 436–439.

[5] A. Momose, T. Takeda, Y. Itai, K. Hirano, Phase–contrast X–ray computed tomography for observing biological soft tissues, Nat. Med. 2 (1996) 473–475.

[6] H. Jiang, Computed Tomography, : Principles, Design, Artifacts, and Recent Advances, second edition, SPIE Press, Bellingham, USA, 2009.

[7] N. Tzourio-Mazoyer, B. Landeau, D. Papathanassiou, F. Crivello, O. Etard, et al., Automated anatomical labeling of activations in SPM using a macroscopic anatomical parcellation of the MNI MRI single-subject brain, Neuroimage 15 (2002) 273–289.

[8] S.G. Kulkarni, X.-L. Gao, S.E. Horner, J.Q. Zheng, N.V. David, Ballistic helmets

−Their design, materials, and performance against traumatic brain injury, Compos. Struct. 101 (2013) 313–331.

[9] H. Mehboob, S.H. Chang, Evaluation of the development of tissue phenotypes: bone fracture healing using functionally graded material composite bone plates, Compos. Struct. 117 (2014) 105–113.

[10] P.J. Basser, C. Pierpaoli, Microstructural and physiological features of tissues elucidated by quantitative-diffusion-tensor MRI, J. Magn. Res. 213 (2011) 560–570.

[11] K.R.A. Van Dijk, M.R. Sabuncu, R.L. Buckner, The influence of head motion on intrinsic functional connectivity MRI, Neuroimage 59 (2012) 431–438.

[12] A.D.B.L. Ferreira, P.R.O. Nóvoa, A.T. Marques, Multifunctional material systems: a state-of-the-art review, Compos. Struct. 151 (2016) 3–35.

[13] J.V. Pardo, P.T. Fox, M.E. Raichle, Localization of a human system for sustained attention by positron emission tomography, Nature 349 (1991) 61–64.

[14] A.F.C. Okines, A.R. Norman, P. McCloud, Y.K. Kang, D. Cunningham, Meta-analysis of the REAL-2 and ML17032 trials: evaluating capecitabine-based combination chemotherapy and infused 5-fluorouracil-based combination chemotherapy for the treatment of advanced oesophago-gastric cancer, Ann. Oncol. 20 (2009) 1529–1534.

[15] J.O. Rinne, D.J. Brooks, M.N. Rossor, N.C. Fox, R. Bullock, et al., 11 C-PiB PET assessment of change in fibrillar amyloid-β load in patients with Alzheimer's disease treated with bapineuzumab: a phase 2, double-blind, placebo-controlled, ascending-dose study, Lancet Neurol. 9 (2010) 363–372.

[16] G. Oliveri, L. Poli, P. Rocca, A. Massa, Bayesian compressive optical imaging within the Rytov approximation, Opt. Lett. 37 (2012) 1760–1762.

[17] A. Grinvald, E. Lieke, R.D. Frostig, C.D. Gilbert, T.N. Wiesel, Functional architecture of cortex revealed by optical imaging of intrinsic signals, Nature 324 (1986) 361–364.

[18] M. Endrizzi, B.I.S. Murat, P. Fromme, A. Olivo, Edge-illumination X-ray dark-field imaging for visualising defects in composite structures, Compos. Struct. 134 (2015) 895–899.

[19] V. Ntziachristos, Going deeper than microscopy: the optical imaging frontier in biology, Nat. Meth 7 (2010) 603–614.

[20] T.L. Szabo, J. Wu, A model for longitudinal and shear wave propagation in viscoelastic media, J. Acoust. Soc. Am. 107 (2000) 2437–2446.

[21] T.L. Szabo, Time domain wave equations for lossy media obeying a frequency power law, J. Acoust. Soc. Am. 96 (1994) 491–500.

[22] W. Chen, S. Holm, Modified Szabo's wave equation models for lossy media obeying frequency power law, J. Acoust. Soc. Am. 114 (2003) 2570–2574.

[23] J. Opretzka, M. Vogt, H. Ermert, A high-frequency ultrasound imaging system combining limited-angle spatial compounding and model-based synthetic aperture focusing, IEEE Trans. Ultrason. Ferroelectr. Freq .Control 58 (2011) 1355–1365.

[24] B. Yuan, S. Uchiyama, Y. Liu, K.T. Nguyen, G. Alexandrakis, High-resolution imaging in a deep turbid medium based on an ultrasound-switchable fluorescence technique, Appl. Phys. Lett. 101 (2012) 033703.

[25] M. Hoehn, E. Küstermann, J. Blunk, D. Wiedermann, T. Trapp, et al., Monitoring of implanted stem cell migration in vivo: a highly resolved in vivo magnetic resonance imaging investigation of experimental stroke in rat, Proc. Natl. Acad. Sci. U. S. A. 99 (2002) 16267–16272.

[26] N. Fang, H. Lee, C. Sun, X. Zhang, Sub-diffraction-limited optical imaging with a silver superlens, Science 308 (2005) 534–537.

[27] T. Beyer, D.W. Townsend, T. Brun, P.E. Kinahan, M. Charron, et al., For clinical oncology, J. Nucl. Med. 41 (2000) 1369–1379.

[28] P.E. Kinahan, D.W. Townsend, T. Beyer, D. Sashin, Attenuation correction for a combined 3D PET/CT scanner, Med. Phys. 25 (1998) 2046.

[29] P.G. Kluetz, C.C. Meltzer, V.L. Villemagne, P.E. Kinahan, S. Chander, Combined PET/CT imaging in oncology: impact on patient management, Clin. Positron Imaging 3 (2000) 223–230.

[30] R. Boellaard, M.J. O'Doherty, W.A. Weber, F.M. Mottaghy, M.N. Lonsdale, et al., FDG PET and PET/CT: EANM procedure guidelines for tumour PET imaging: version 1.0, Eur. J. Nucl. Med. Mol. Imaging 37 (2010) 181–200.

[31] M.S. Judenhofer, H.F. Wehrl, D.F. Newport, C. Catana, S.B. Siegel, et al., Simultaneous PET-MRI: a new approach for functional and morphological imaging, Nat. Med. 14 (2008) 459–465.

[32] B.J. Pichler, M.S. Judenhofer, C. Catana, J.H. Walton, M. Kneilling, et al., Performance test of an LSO-APD detector in a 7-T MRI scanner for simultaneous PET/MRI, J. Nucl. Med. 47 (2006) 639–647.

[33] B.J. Pichler, A. Kolb, T. Nägele, H. Schlemmer, PET/MRI: paving the way for the next generation of clinical multimodality imaging applications, J. Nucl. Med. 51 (2010) 333–336.

[34] A. Boss, S. Bisdas, A. Kolb, M. Hofmann, U. Ernemann, et al., Hybrid PET/MRI of intracranial masses: initial experiences and comparison to PET/CT, J. Nucl. Med. 51 (2010) 1198–1205.

[35] N.M. Alpert, D. Berdichevsky, Z. Levin, E.D. Morris, A.J. Fischman, Improved methods for image registration, Neuroimage 3 (1996) 10–18.

[36] E.M. Blanchet, C. Millo, V. Martucci, Integrated whole-body PET/MRI with 18F-FDG, 18F-FDOPA, and 18F-FDA in paragangliomas in comparison with PET/CT: NIH first clinical experience with a single-injection, dual-modality imaging protocol, Clin. Nucl. Med. 39 (2014) 243–250.

[37] H. Xu, R. Springett, H. Dehghani, B.W. Pogue, K.D. Paulsen, et al., Magnetic-resonance-imaging–coupled broadband near-infrared tomography system for small animal brain studies, Appl. Opt. 44 (2005) 2177–2188.

[38] H.E. Daldrup-Link, M. Rudelius, S. Metz, G. Piontek, B. Pichler, et al., Cell tracking with gadophrin-2: a bifunctional contrast agent for MR imaging, optical imaging, and fluorescence microscopy, Eur. J. Nucl. Med. Mol. Imaging 31 (2004) 1312–1321.

[39] W.J.M. Mulder, R. Koole, R.J. Brandwijk, G. Storm, P.T.K. Chin, et al., Quantum dots with a paramagnetic coating as a bimodal molecular imaging probe, Nano Lett. 6 (2006) 1–6.

[40] D.K. Yi, S.T. Selvan, S.S. Lee, G.C. Papaefthymiou, D. Kundaliya, J.Y. Ying, Silica-coated nanocomposites of magnetic nanoparticles and quantum dots, J. Am. Chem. Soc. 127 (2005) 4990–4991.

[41] A. Kale, S. Kale, P. Yadav, H. Gholap, R. Pasricha, J.P. Jog, B. Lefez, B. Hannoyer, P. Shastry, S. Ogaleet, Magnetite/CdTe magnetic-fluorescent composite nanosystem for magnetic separation and bio-imaging, Nanotech 22 (2011) 225101.

[42] K.W. Kwon, M. Shim, γ-Fe₂O₃/II-VI sulfide nanocrystal heterojunctions, J. Am. Chem. Soc. 127 (2005) 10269–10275.

[43] J. Gao, W. Zhang, P. Huang, B. Zhang, X. Zhang, B. Xu, Intracellular spatial control of fluorescent magnetic nanoparticles, J. Am. Chem. Soc. 130 (2008) 3710–3711.

[44] S.F. Chin, K.S. Iyer, C.L. Raston, Facile and green approach to fabricate gold and silver coated superparamagnetic nanoparticles, Cryst. Growth Des. 9 (2009) 2685–2689.

[45] Z. Xu, Y. Hou, S. Sun, Magnetic core/shell Fe₃O₄/Au and Fe₃O₄/Au/Ag nanoparticles with tunable plasmonic properties, J. Am. Chem. Soc. 129 (2007) 8698–8699.

[46] F. Liu, S. Laurent, A. Roch, L.Vander Elst, R.N. Muller, Size-controlled synthesis of CoFe₂O₄ nanoparticles potential contrast agent for MRI and investigation on their size-dependent magnetic properties, J. Nanomater. 2013 (2013) 127.

[47] A. Zur, T.C. McGill, Lattice match: an application to heteroepitaxy, J. Appl. Phys. 55 (1984) 378–386.

[48] G. Friedel, Lacons De Cristallographie, Berger Levrault, Paris,French, 1926.

[49] P.H. Pumphrey, Grain Boundary Structure and Properties, Academic London, UK, 1976.

[50] K.C. Lee, U. Erb, Grain boundaries and coincidence site lattices in the corneal nanonipple structure of the Mourning Cloak butterfly, J. Nanotechnol. 4 (2013) 292–299.

[51] M.J.C. Loquias, P. Zeiner, Colourings of lattices and coincidence site lattices, Philos. Mag. 91 (2011) 2680–2689.

[52] V. Blaskov, V. Petkov, V. Rusanov, L.M. Martinez, B. Martinez, et al., Magnetic properties of nanophase CoFe₂O₄ particles, J. Magn. Magn. Mater. 162 (1996) 331–337.

[53] G.I. Tóth, G. Tegze, T. Pusztai, L. Gránásy, Heterogeneous crystal nucleation: the effect of lattice mismatch, Phys. Rev. Lett. 108 (2012) 025502.

[54] T. Sen, S.J. Sheppard, T. Mercer, M. Eizadi-Sharifabad, M. Mahmoudief, Simple one-pot fabrication of ultra-stable core-shell superparamagnetic nanoparticles for potential application in drug delivery, RSC Adv. 2 (2012) 5221–5228.

[55] C. Cannas, A. Musinu, A. Ardu, F. Orru, D. Peddis, et al., CoFe₂O₄ and CoFe₂O₄/SiO₂ core/shell nanoparticles: magnetic and spectroscopic study, Chem. Mater. 22 (2010) 3353–3361.

[56] C.M.B. Santos, S.W. da Silva, L.R. Guilherme, P.C. Morais, SERRS study of molecular arrangement of amphotericin B adsorbed onto iron oxide nanoparticles precoated with a bilayer of lauric acid, J. Phys. Chem. 115 (2011) 20442–20448.

[57] Z. Bai, L. Yang, J. Zhang, L. Li, C. Hu, High-efficiency carbon-supported platinum catalysts stabilized with sodium citrate for methanol oxidation, J. Power Sources 195 (2010) 2653–2658.

[58] V. Vila, J.A. Aznar, A. Moret, A. Marco, S. Navarro, Assessment of the thrombin generation assay in haemophilia: comparative study between fresh and frozen platelet-rich plasma, Haemophilia 19 (2013) 318–321.

[59] M. Younas, M. Nadeem, M. Atif, R. Grossinger, Metal-semiconductor transition in NiFe₂O₄ nanoparticles due to reverse cationic distribution by impedance spectroscopy, J. Appl. Phys. 109 (2011) 093704.

[60] C. Cannas, A. Musinu, G. Piccaluga, D. Fiorani, D. Peddis, Magnetic properties of cobalt ferrite-silica nanocomposites prepared by a sol-gel autocombustion technique, J. Chem. Phys. 125 (2006) 164714.

[61] G. Concas, G. Spano, C. Cannas, A. Musinu, D. Peddis, Inversion degree and saturation magnetization of different nanocrystalline cobalt ferrites, J. Magn. Magn. Mater. 321 (2009) 1893–1897.

[62] G.A. Sawatzky, F. Van der Woude, A.H. Morrish, Recoilless-fraction ratios for Fe 57 in octahedral and tetrahedral sites of a spinel and a garnet, Phys. Rev. 187 (1969) 747–757.

[63] D.A. Yablonskiy, E.M. Haacke, Theory of NMR signal behavior in magnetically inhomogeneous tissues: the static dephasing regime, Magn. Reson. Med. 32 (1994) 749–763.

[64] F. Liu, S. Laurent, L. Vander Elst, R.N. Muller, Synthesis of CdTe QDs by hydrothermal method, with tunable emission fluorescence, Mater Res Expr 2 (2015) 095901.

[65] F. Abraham, Homogeneous Nucleation Theory: The Pretransition Theory of Vapor Condensation, Academic Pr, Waltham, Massachusetts, USA, 1973.

[67] D.C. Zhu, R.D. Penn, Full-brain T1 mapping through inversion recovery fast spin echo imaging with time-efficient slice ordering, Magn. Reson. Med. 54 (2005) 725–731.

[68] J.H. Kim, C.H. Lee, S.K. Lee, Superparamagnetic Gd-and Mn-substituted magnetite fluids applied as MRI contrast agents, Bull. Korean Chem. Soc. 30 (2009) 1305–1308.

[69] Y.L. Lin, A.P. Koretsky, Manganese ion enhances T1-weighted MRI during brain activation: an approach to direct imaging of brain function, Magn. Res. Med. 38 (1997) 378–388.

[70] E. Vinogradov, H. He, A. Lubag, J.A. Balschi, A.D. Sherry, MRI detection of paramagnetic chemical exchange effects in mice kidneys in vivo, Magn. Res. Med. 58 (2007) 650–655.